International Journal of Civil Engineering (2023) 21:839–855
https://doi.org/10.1007/s40999-022-00800-6

RESEARCH PAPER

A Diagnostic Method Based on Deflection Analysis for Monitoring Post-elastic Response of Beams

Adam Sciegaj[1,2]

Received: 21 January 2022 / Revised: 30 November 2022 / Accepted: 23 December 2022 / Published online: 30 January 2023

Abstract

A non-destructive diagnostic method based on deflection analysis for monitoring the post-elastic response of beams was developed, and a diagnostic indicator was proposed. The indicator was defined as the second moment of the normalised curvature function about the mid-span, where the curvature was computed from the normalised deflection function. Elastic reference values of the indicator were computed for simply supported beams under uniformly distributed load, three-point, and four-point bending. Development of the indicator under progressive loading was examined with the help of finite element analyses. The indicator value monotonically decreased with increasing deformation provided that maximum bending moment was located between $0.41L$ and $0.59L$, where L is the span of the beam. In this interval, the value of the indicator was unique and enabled the direct monitoring of the post-elastic stress level in the cross-section. The method was validated with the help of available experiments on simply supported beams. For beams working in the elastic range, a mean error of 2.1% was obtained between the measured and theoretical indicator values. For quasi-brittle material in the post-elastic stage, the decreasing value of the indicator signified the development of damage in accordance with experimental results.

Keywords Deflection analysis · Structural health monitoring · Beam · Curvature · Elastoplastic · Damage

1 Introduction

All engineering structures undergo deformations during their lifetime due to external loads and environmental conditions. Accidental loads (e.g., earthquakes) and impact loads may lead to excessive deformation of a structure or its components, thus causing localised damage, including cracks in quasi-brittle materials. In beam structures made of elastoplastic materials, loads larger than the elastic limit load result in the formation of plastic hinges, which, in turn, may lead to the failure of structural components if the deformation is considerably large. Furthermore, many experiments performed in a controlled environment, such as the bending test, often involve large deformations and loading of the structure beyond the elastic range. Deflection function of the beam can provide useful information on the state of the structure. Detailed analytical and numerical evaluation of the post-elastic response of beams is not trivial [1–3]. In case of bridges, influence lines can be used to detect damage [4]. Thus, examining the post-elastic state of the structure undergoing deformations is crucial.

Structural health monitoring (SHM) systems can be employed to measure displacements in the structure both in-situ and during laboratory tests. Various techniques are suitable for direct displacement measurement, i.e., methods based on a linear variable differential transformer (LVDT) [5], laser Doppler vibrometer [6], fibre-optic sensors (FOS) [7–13], digital image correlation (DIC) [14–17], vision-based monitoring [18–22] and terrestrial laser scanning (TLS) [23, 24]. Displacements can also be indirectly determined by the adequate treatment of measured strains and accelerations [25] and instrumentation of a passing vehicle [26]. In the case of beam structures, deflection

---

✉ Adam Sciegaj
adam.sciegaj@pg.edu.pl

[1] Department of Mechanics of Materials and Structures, Faculty of Civil and Environmental Engineering, Gdańsk University of Technology, Narutowicza 11/12, 80-233 Gdańsk, Poland

[2] EkoTech Center, Gdańsk University of Technology, Narutowicza 11/12, 80-233 Gdańsk, Poland

analysis can be used for damage detection [19, 27–32], stress-state estimation [8, 33], and serviceability assessment [34, 35]. However, no study has comprehensively monitored the elastoplastic response of beam structures.

In this work, the first step is taken towards the development of a simple non-destructive diagnostic method for monitoring post-elastic behaviour of beam structures. This is done by computing a diagnostic indicator based on the curvature function and relating its value to the elastic reference value. Although the presented methodology can be generalised to arbitrary support and loading conditions, the analysis in this work was limited to simply supported beams under uniformly distributed load, as well as those in three- and four-point bending. Moreover, it was assumed that structural geometry of the beam allows for its efficient mathematical modelling according to Euler–Bernoulli assumptions. The novelty of the proposed method lies in its simplicity because no additional information apart from that on the shape of the deflection line is required to determine whether the beam has entered the post-elastic range.

The remainder of this paper is structured as follows. Section 2 presents the general procedure of computing the diagnostic indicator and reports the elastic reference values of the indicator. Section 3 describes the finite element analyses used to study the development of the diagnostic indicator in elastoplastic range. The method is further validated with help of available experimental data in Sect. 4, where real structures working in the elastic range are studied. The method is also employed to detect the onset and monitor the development of damage in quasi-brittle material. In addition, Sect. 4 discusses some practical aspects and guidelines on efficient implementation. The paper is concluded in Sect. 5 with some final remarks.

2 Diagnostic Framework

Let us consider a simply supported beam with a span of L, as shown in Fig. 1. It is assumed that the real deflection function, $w(x)$, where x ranges from 0 to L, is known either in its analytical form, or measured data points are available. In the following, a positive deflection w is considered upwards in Fig. 1. First, we perform the coordinate substitution $\xi = \frac{x}{L}$, such that the coordinate ξ ranges from 0 to 1. In the next step, we rescale the deflection values (min-max normalisation) such that the values of $\bar{w}(\xi)$ lie between 0 and ± 1, i.e.,

$$\bar{w}(\xi) = \frac{w(\xi) - \min(|w(\xi)|)}{\max(|w(\xi)|) - \min(|w(\xi)|)}, \tag{1}$$

where the absolute values ensure that the rescaling is valid for both positive and negative deflection values. The normalised deflection function is then used to compute the curvature, $\kappa(\xi)$, according to the definition

$$\kappa(\xi) = \frac{\left|\dfrac{\mathrm{d}^2\bar{w}(\xi)}{\mathrm{d}\xi^2}\right|}{\left(1 + \left(\dfrac{\mathrm{d}\bar{w}(\xi)}{\mathrm{d}\xi}\right)^2\right)^{3/2}}. \tag{2}$$

The curvature function is then normalised such that its value ranges from 0 to 1

$$\bar{\kappa}(\xi) = \frac{\kappa(\xi) - \min(\kappa(\xi))}{\max(\kappa(\xi)) - \min(\kappa(\xi))} = \frac{\kappa(\xi)}{\max(\kappa(\xi))}, \tag{3}$$

where it was used that the curvature computed from Eq. 2 is non-negative and its minimum is 0. The normalisation exhibits two notable features of the method. First, as long as the external load does not exceed the elastic limit load, $\bar{w}(\xi)$ and $\bar{\kappa}(\xi)$ will not change. Thus, exact monitoring whether the beam is in the elastic range, is possible. Second, a meaningful comparison between different beams can be performed because $\bar{\kappa}$ will be in the same range for all cases. It is now possible to introduce the *diagnostic indicator*, which is chosen as the second moment of $\bar{\kappa}(\xi)$ about the mid-span of the beam, i.e.,

$$\mu_2 = \int_0^1 (\xi - 0.5)^2 \; \bar{\kappa}(\xi) \; \mathrm{d}\xi. \tag{4}$$

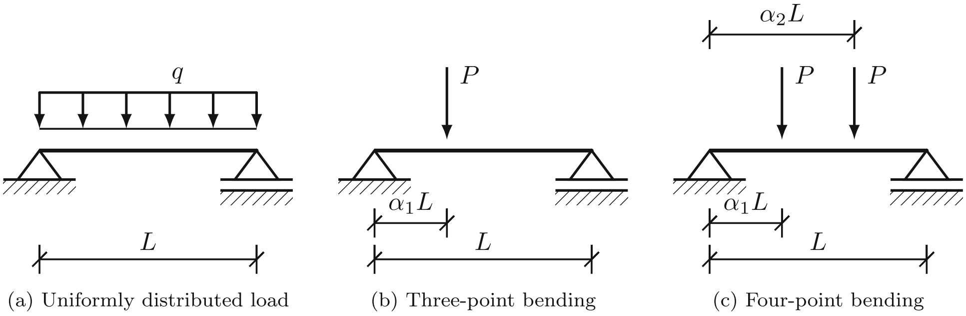

(a) Uniformly distributed load (b) Three-point bending (c) Four-point bending

Fig. 1 Studied load cases of simply supported Euler–Bernoulli beams

2.1 Uniformly Distributed Load—Elastic Reference Value

For a simply supported Euler–Bernoulli beam with length L under a uniformly distributed load q (cf. Fig. 1a), the deflection function can be expressed as

$$w(x) = -\frac{qL^4}{24EI}\left(\frac{x^4}{L^4} - 2\frac{x^3}{L^3} + \frac{x}{L}\right), \tag{5}$$

where EI denotes the bending stiffness. Given the absolute value of the maximum elastic deflection is $\frac{5qL^4}{384EI}$ in the mid-span, the normalised deflection function can be expressed as:

$$\bar{w}(\xi) = -3.2\left(\xi^4 - 2\xi^3 + \xi\right). \tag{6}$$

With the help of Eq. 2, the curvature can be calculated as

$$\kappa(\xi) = \frac{|38.4\ \xi(\xi-1)|}{\left(1 + 10.24\left(4\xi^3 - 6\xi^2 + 1\right)^2\right)^{3/2}}. \tag{7}$$

Because the maximum curvature can be found at $\xi = 0.5$, $\kappa(\xi)$ can be normalised as

$$\bar{\kappa}(\xi) = \frac{\kappa(\xi)}{\kappa(0.5)} = \frac{|4\ \xi(\xi-1)|}{\left(1 + 10.24\left(4\xi^3 - 6\xi^2 + 1\right)^2\right)^{3/2}}. \tag{8}$$

The resulting normalised curvature function is a bell-shaped curve, which is plotted along the normalised deflection function for a quick reference in Fig. 2. Finally, the elastic reference value of the diagnostic indicator is computed as

$$\mu_{2,el} = \int_0^1 \frac{(\xi-0.5)^2|4\ \xi(\xi-1)|}{\left(1 + 10.24\left(4\xi^3 - 6\xi^2 + 1\right)^2\right)^{3/2}} \mathrm{d}\xi = 2.477 \times 10^{-3}. \tag{9}$$

2.2 Three-Point Bending—Elastic Reference Value

For a simply supported Euler–Bernoulli beam with length L loaded with external force P at distance $\alpha_1 L$ from the support (see Fig. 1b), the deflection function can be expressed as

$$w(\xi,\alpha_1) = \begin{cases} -\frac{PL^3}{6EI}(1-\alpha_1)\left(\left(1-(1-\alpha_1)^2\right)\xi - \xi^3\right) & \text{if } \xi \le \alpha_1, \\ -\frac{PL^3}{6EI}\alpha_1\left(\left(1-\alpha_1^2\right)(1-\xi) - (1-\xi)^3\right) & \text{if } \xi > \alpha_1. \end{cases} \tag{10}$$

Restricting to $\alpha_1 \ge 0.5$ due to symmetry, the absolute value of the maximum deflection is

$$w\mathrm{max} = \frac{PL^3}{9EI}\alpha_1^2(1-\alpha_1)(2-\alpha_1)\sqrt{\frac{2-\alpha_1}{3\alpha_1}}, \tag{11}$$

and the normalised deflection can be expressed as

$$\bar{w}(\xi,\alpha_1) = \begin{cases} -\frac{3\left(\left(1-(1-\alpha_1)^2\right)\xi - \xi^3\right)}{2\alpha_1^2(2-\alpha_1)\sqrt{\frac{2-\alpha_1}{3\alpha_1}}} & \text{if } \xi \le \alpha_1, \\ -\frac{3\left(\left(1-\alpha_1^2\right)(1-\xi) - (1-\xi)^3\right)}{2\alpha_1(1-\alpha_1)(2-\alpha_1)\sqrt{\frac{2-\alpha_1}{3\alpha_1}}} & \text{if } \xi > \alpha_1. \end{cases} \tag{12}$$

For brevity, the exact analytical derivation of the curvature, $\kappa(\xi)$, and normalised curvature, $\bar{\kappa}(\xi)$, is skipped in the following. Depending on α_1, the elastic reference value of the diagnostic indicator is computed and presented in Fig. 3 with exact numerical values reported in Table 2. The graph is symmetric about the mid-span, as fundamentally there is no difference on which side of the beam the load is applied.

2.3 Four-Point Bending—Elastic Reference Value

Next, a simply supported Euler–Bernoulli beam in four-point bending was examined (Fig. 1c). The beam has a

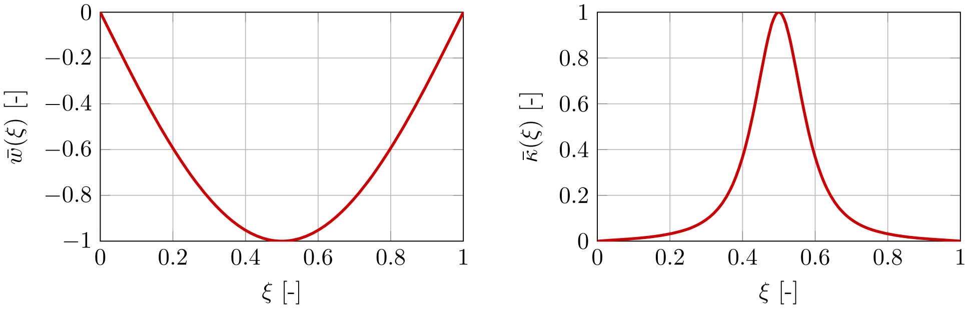

Fig. 2 Normalised deflection (left) and curvature (right) functions for the case of uniformly distributed load

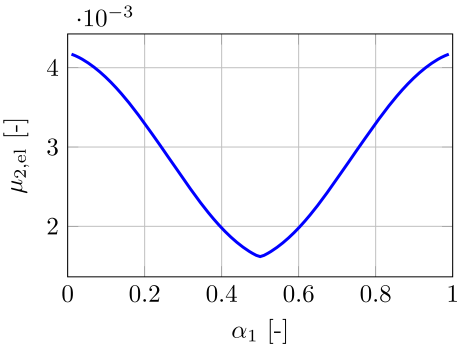

Fig. 3 Elastic reference value of the diagnostic indicator, $\mu_{2,el}$, as a function of load location, α_1, for the case of three-point bending

length L and is loaded with two external forces of the same magnitude P at $\alpha_1 L$ and $\alpha_2 L$ from the left support. For simplicity, it is assumed that $(\alpha_1, \alpha_2) \in (0,1) \times (0,1)$. As the four-point bending problem is a superposition of two independent three-point bending problems, the deflection function will be a sum of the functions in Eq. 10, i.e.,

$$w(\xi, \alpha_1, \alpha_2) = \begin{cases} -\frac{PL^3}{6EI}[(1-\alpha_1)\left(\left(1-(1-\alpha_1)^2\right)\xi - \xi^3\right) + \\ \quad (1-\alpha_2)\left(\left(1-(1-\alpha_2)^2\right)\xi - \xi^3\right)] \qquad \text{if } \xi \le \alpha_1, \\ -\frac{PL^3}{6EI}[\alpha_1\left((1-\alpha_1^2)(1-\xi) - (1-\xi)^3\right) + \\ \quad (1-\alpha_2)\left(\left(1-(1-\alpha_2)^2\right)\xi - \xi^3\right)] \qquad \text{if } \alpha_1 < \xi \le \alpha_2, \\ -\frac{PL^3}{6EI}[\alpha_1\left((1-\alpha_1^2)(1-\xi) - (1-\xi)^3\right) + \\ \quad \alpha_2\left((1-\alpha_2^2)(1-\xi) - (1-\xi)^3\right)] \qquad \text{if } \xi > \alpha_2, \end{cases} \tag{13}$$

For brevity, the analytical details of curvature computation are omitted. The elastic reference values of the diagnostic indicator, $\mu_{2,el}$ are presented in Fig. 4, with the exact numerical values of $\mu_{2,el}$ reported in Table 3. By examining contour and surface plots, it can be seen that the graph from Fig. 3 is a slice of the surface along the diagonal as well as along the horizontal and vertical axes. This is expected, as in these cases the problem effectively reduces to three-point bending.

3 Diagnostic Indicator Development in the Elastoplasic Range

To study the devised diagnostic scheme in the elastoplastic range, finite element analysis was utilised. To this end, simply supported beams were modelled in the commercial finite element code Abaqus. Beams had the length $L = 3$m and a square cross-section with a side length of 0.1m; thus, the span-to-depth ratio justified using the Euler–Bernoulli model. A perfect elastoplastic material with Young's modulus $E = 200\,$GPa and a yield stress of 350 MPa was considered. Each beam was modelled with $l_e = 0.005\,$m long Euler–Bernoulli beam elements (a total of 600 elements along the beam). The beams were then progressively loaded, and vertical displacements were extracted for all nodes. At each loading step, the deflection function was reconstructed, and the diagnostic indicator was computed. In addition, the bending moment ratio, M/M_{el}, and the deflection ratio, δ/δ_{el}, relating current and elastic values were computed. The elastic bending moment, M_{el}, refers to the maximum bending moment under the elastic limit load, i.e., when stresses at the outermost cross-section fibres reach the yield stress. Similarly, the elastic deflection, δ_{el}, refers to the deflection at the location of the maximum moment when the beam is loaded with the elastic limit load. The natural logarithm of the indicator ratio, $\ln\frac{\mu_{2,el}}{\mu_2}$, relates the elastic reference value of the diagnostic indicator to its current value.

3.1 Uniformly Distributed Load

In the first study, the beam was loaded with a uniformly distributed load. The analysis was run in arc-length control, increasing the distributed load until the mid-span displacement reached a preset value. The development of the diagnostic indicator and the indicator ratio under load is presented in Fig. 5, with both M_{el} and δ_{el} computed at the mid-span. The normalised deflection and curvature profiles at selected load steps are presented in Fig. 6.

The response can be divided into three separate regions. First, the elastic range can be identified by the horizontal part of the left curve, where the value of the indicator is equal to its elastic reference value, i.e., $\mu_2 = \mu_{2,el} = 2.477 \times 10^{-3}$. Until δ_{el} (or M_{el}), this value is constant, and the logarithm of the indicator ratio is 0 (indicating that the ratio is 1). In this region, the normalised deflection and curvature functions do not change. As soon as the yield stress is reached at the outermost fibres of the cross-section, the interior of the bell-shaped curvature function becomes slightly thinner, particularly around inflection points, and the value of the indicator starts decreasing. After the mid-span section has fully plasticised, the curvature profile starts to form a sharp peak in the middle. This causes a significant decrease in the indicator value, and a rapid increase in the indicator ratio. The moment ratio remains constant at 1.5 (as expected for a square cross-section) as the plastic limit load is reached. In this case, as plastic hinge formed in the mid-span and in the limit, the indicator value tends to 0.

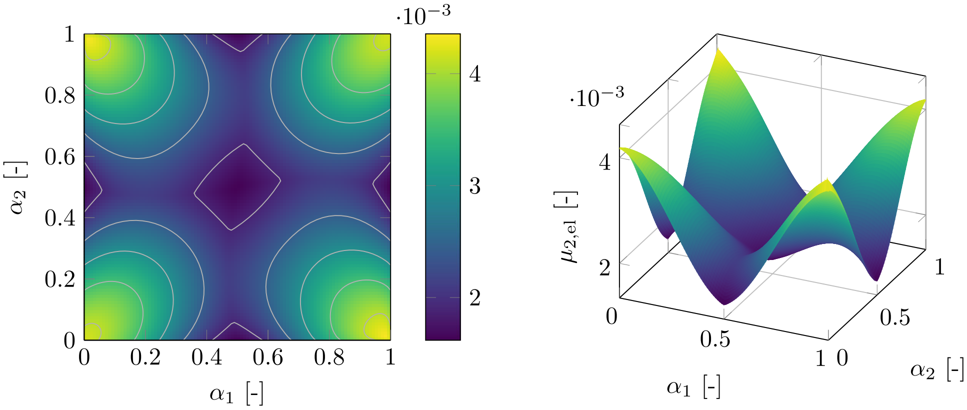

Fig. 4 Contour (left) and the surface (right) of the elastic reference value of the diagnostic indicator, $\mu_{2,el}$ as a function of point load locations, α_1 and α_2, for the case of four-point bending

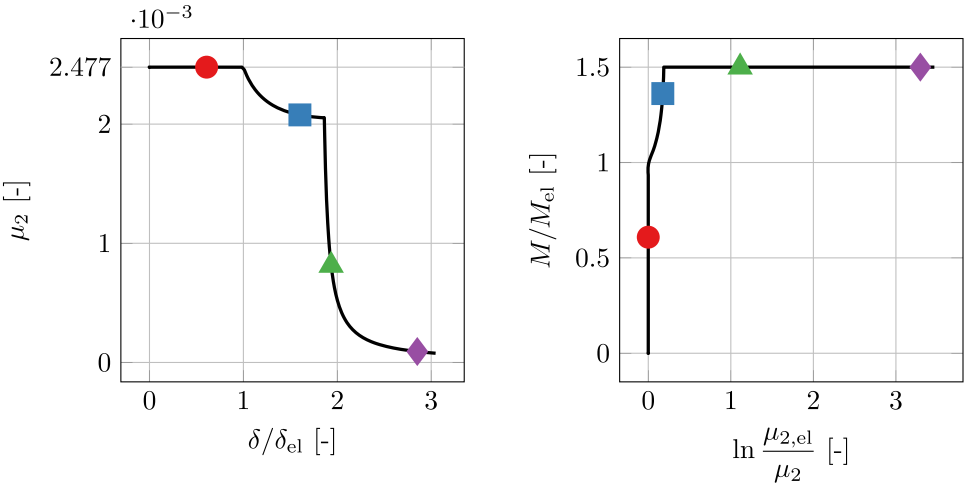

Fig. 5 Development of the diagnostic indicator (left) and bending moment (right) as a function of displacement and indicator ratios for the case of uniformly distributed load

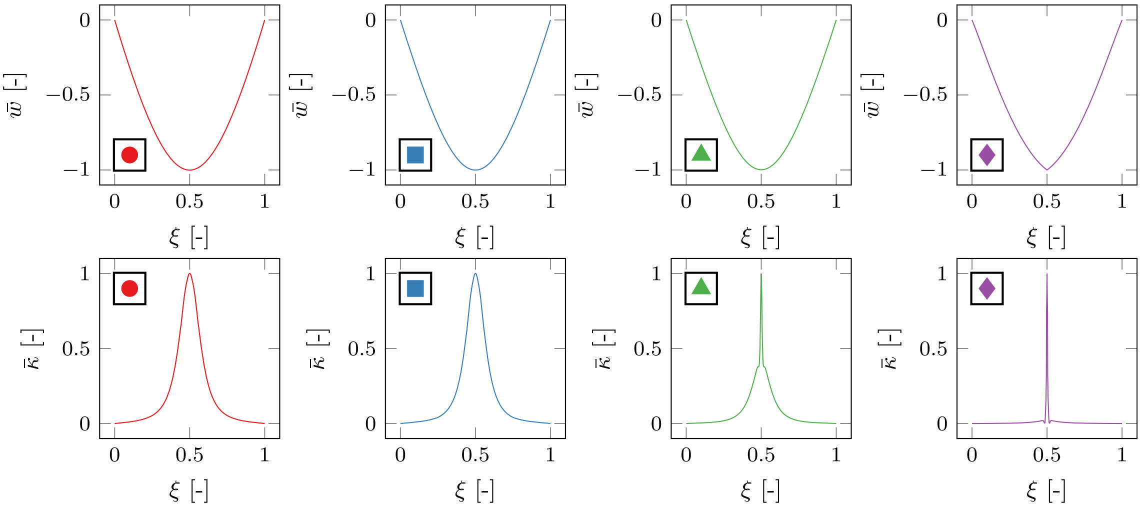

Fig. 6 Normalised deflection, $\bar{w}(\xi)$, and curvature, $\bar{\kappa}(\xi)$, functions at selected load steps for the case of uniformly distributed load

The effect of the cross-section shape on the development of the diagnostic indicator is presented in Fig. 7, where a circular cross-section (radius of 0.06 m), and a thin-walled circular tube (radius of 0.06 m and wall thickness of 0.001 m) were added. Differences can be noticed only after the elastic stage, with plastic-to-elastic bending moment ratios being consistent with theory (1.5 for a square, 1.698 for a circle, and 1.273 for a thin-walled tube). Because the tube is also circular, the two curves develop in the same way directly after the elastic stage.

3.2 Three-Point Bending

In the second study, the previously used square cross-section was considered for a beam loaded with a point force at $\alpha_1 = 0.2$, cf. Fig. 1b. The analysis was performed under displacement control, with the displacement under the force being the control parameter. The behaviour of the diagnostic indicator and the indicator ratio under increasing load is presented in Fig. 8, with both M_{el} and δ_{el} computed at $\xi = 0.2$. Normalised deflection and curvature profiles at selected load steps are presented in Fig. 9.

The indicator starts at the elastic reference value ($\mu_{2,el} = 3.297 \times 10^{-3}$ for $\alpha_1 = 0.2$) and decreases towards the end. However, the behaviour is non-monotonic as it also grows in the intermediate stage. This is caused by the plastic hinge being formed at $\xi = 0.2$, far from the peak of the initial bell-shaped curvature profile (which is located at $\xi = 0.4278$). The peak shifts from the initial elastic position to the final position determined by the largest bending moment. As presented in Fig. 9, the part of the curvature caused by the formation of the plastic hinge grows separately from the main portion of the bell-shaped curve, thus increasing the value of μ_2. Once the normalised curvature at the hinge reaches 1, the value of the indicator starts decreasing rapidly. Although the value tends to 0 in the limit theoretically, due to finite size of the mesh the numerical result will tend to $(0.5 - \alpha_1)^2 l_e$, where l_e is the size of the mesh.

3.3 Four-Point Bending

For the next case, the beam with a square cross-section was loaded with point forces at $\alpha_1 = 0.15$ and $\alpha_2 = 0.7$, cf. Fig. 1c. Equal forces were exerted on the beam by modelling a rigid body in contact with the beam at $\alpha_1 L$ and $\alpha_2 L$. The analysis was performed under displacement control, with the displacement under the rigid body being the control parameter. The behaviour of the diagnostic indicator and the indicator ratio under increasing load is presented in Fig. 10, with both M_{el} and δ_{el} computed at the location of the largest bending moment, i.e., at $\xi = 0.7$ in this case. Normalised deflection and curvature profiles at selected load steps are presented in Fig. 11.

Depending on α_1 and α_2, the function of the diagnostic indicator under increasing load will not, in general, be monotonic. As before, it will start at the elastic reference value, which is now different ($\mu_{2,el} = 2.951 \times 10^{-3}$ for $\alpha_1 = 0.15$ and $\alpha_2 = 0.7$). The plastic hinge will form at either $\alpha_1 L$ or $\alpha_2 L$, depending on where the bending moment is larger. It is noteworthy that when $\alpha_1 + \alpha_2 = 1$, the bending moment is constant in the region $[\alpha_1, \alpha_2]$. The plastic hinge can therefore form at an arbitrary section within the range. In reality, the location of the plastic hinge will be predefined by local defects and structural details. The general behaviour of the indicator under load is similar to three-point bending.

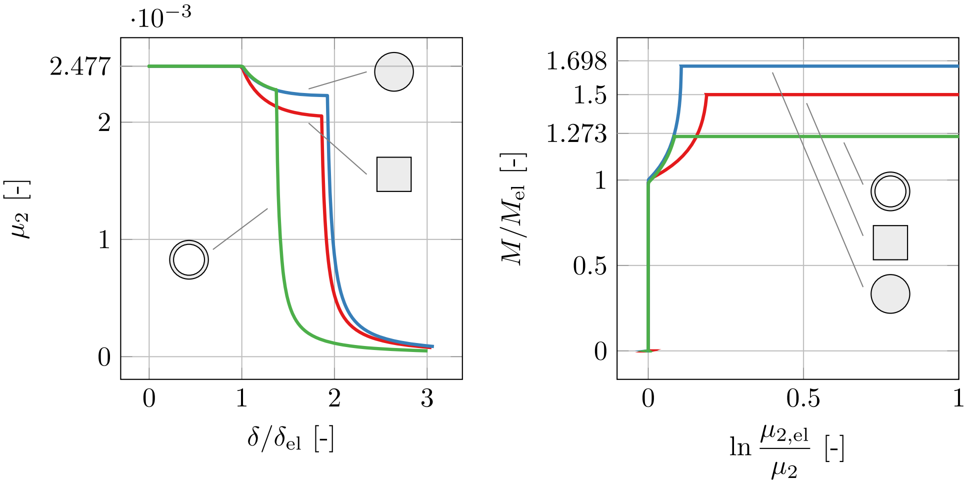

Fig. 7 Development of the diagnostic indicator (left) and bending moment (right) as a function of displacement and indicator ratios for different cross-sectional shapes — uniformly distributed load

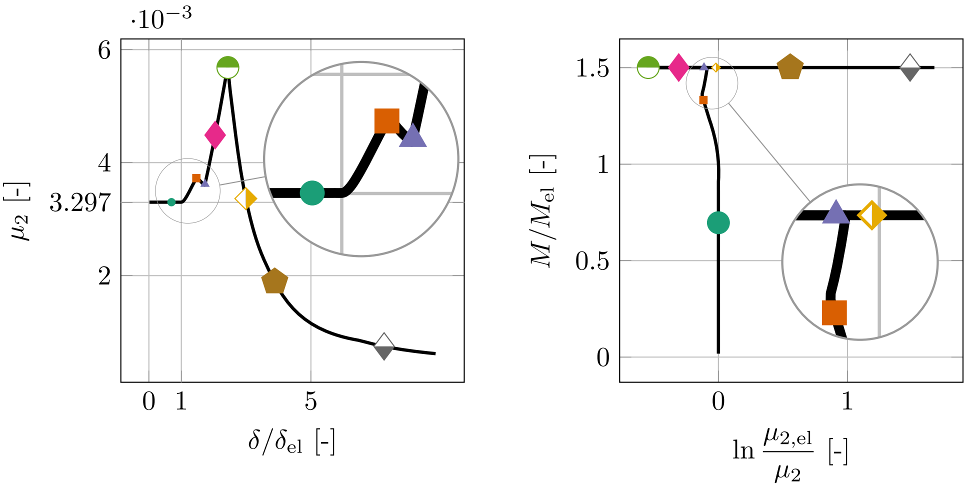

Fig. 8 Development of the diagnostic indicator (left) and bending moment (right) as a function of displacement and indicator ratios for the case of three-point bending with the force at $\alpha_1 = 0.2$

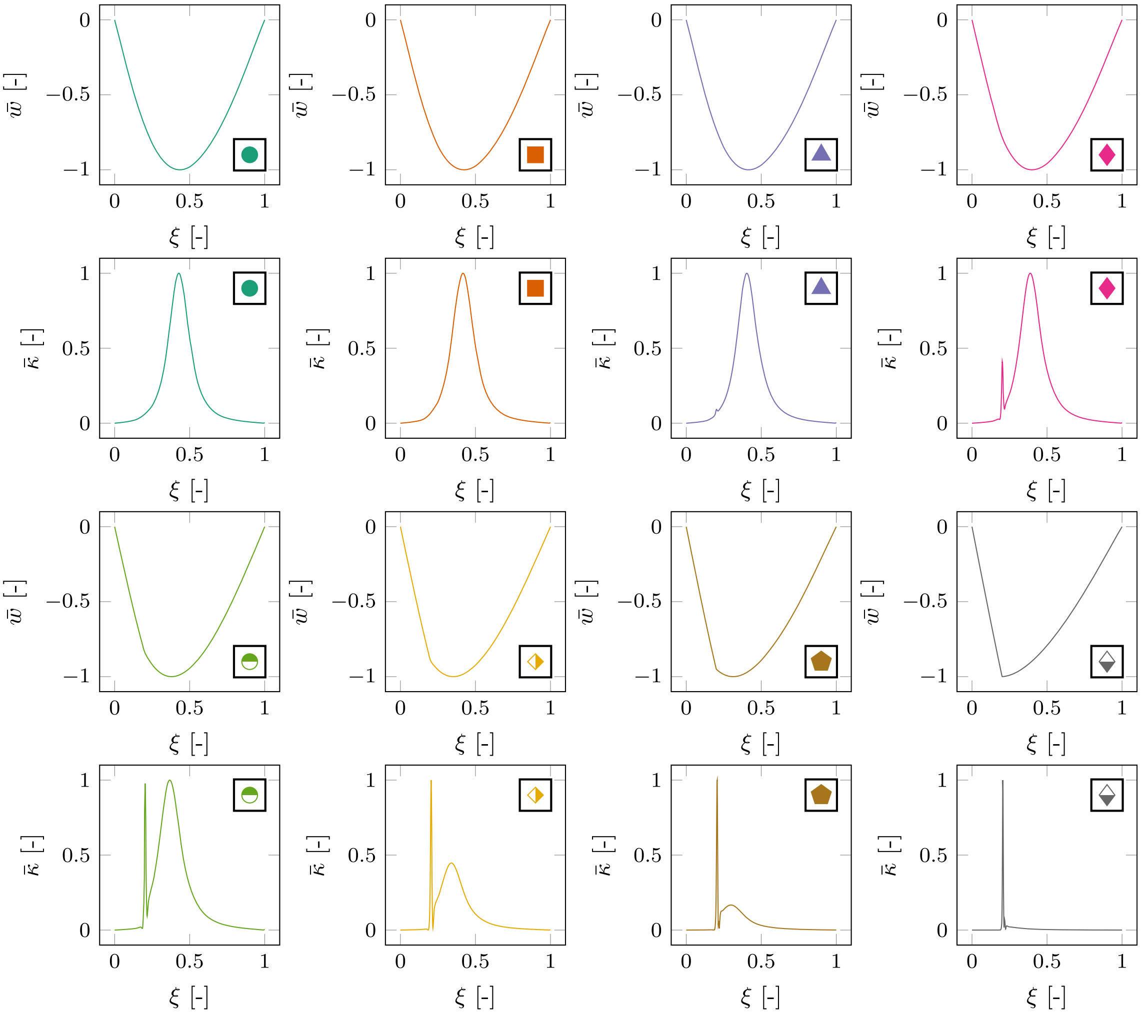

Fig. 9 Normalised deflection,$\bar{w}(\xi)$, and curvature, $\bar{\kappa}(\xi)$, functions at selected load steps for the case of three-point bending with the force at $\alpha_1 = 0.2$

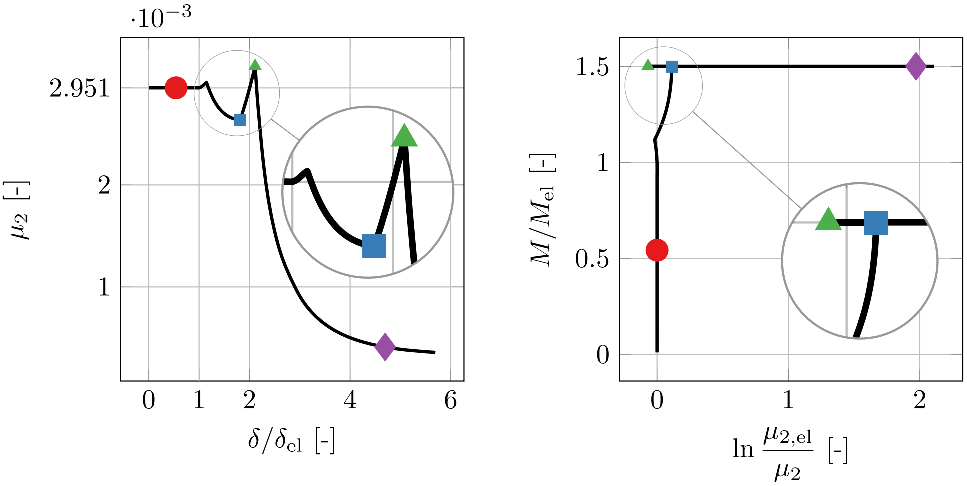

Fig. 10 Development of the diagnostic indicator (left) and bending moment (right) as a function of displacement and indicator ratios for the case of four-point bending with the forces at $\alpha_1 = 0.15$ and $\alpha_2 = 0.7$

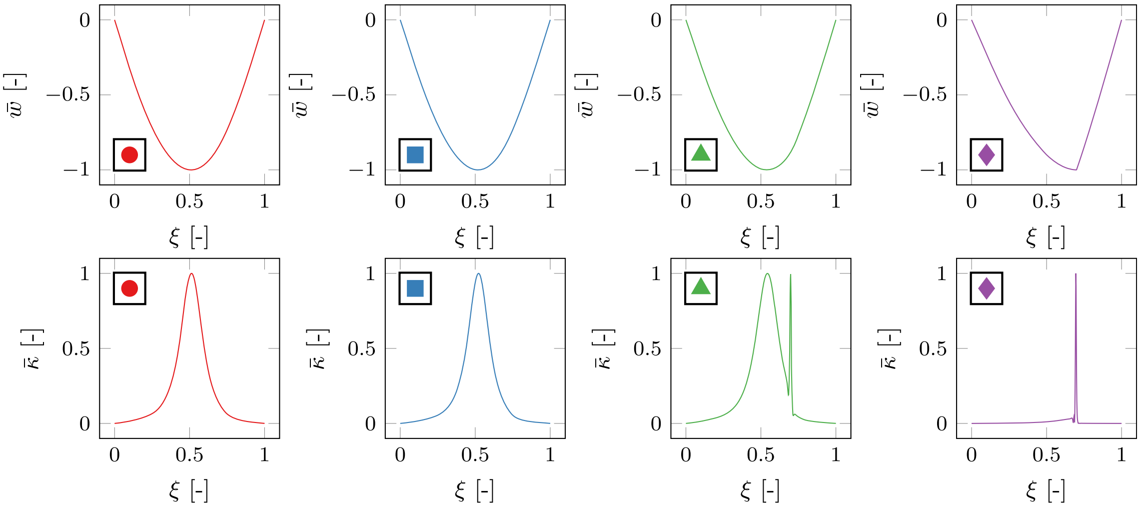

Fig. 11 Normalised deflection,$\bar{w}(\xi)$, and curvature, $\bar{\kappa}(\xi)$, functions at selected load steps for the case of four-point bending with the forces at $\alpha_1 = 0.15$ and $\alpha_2 = 0.7$

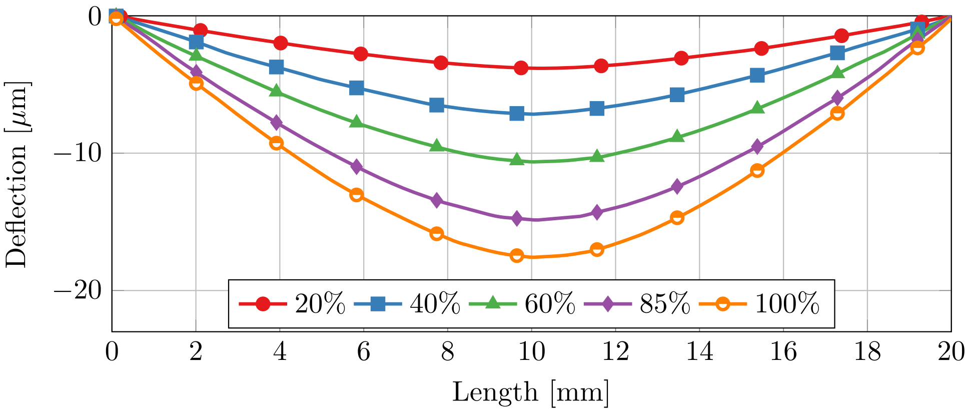

Fig. 12 Deflection profiles at different load levels in the three-point bending test. Data extracted from [38]

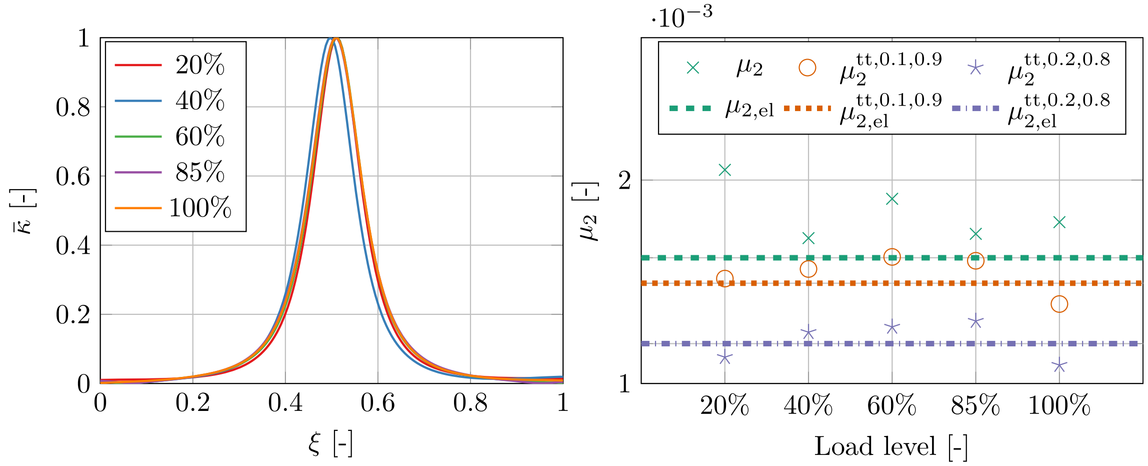

Fig. 13 Normalised curvature, $\bar{\kappa}$ (left), and the computed values of diagnostic indicator, μ_2 together with elastic reference values. Three-point bending test carried out by Farsi et al. [38]

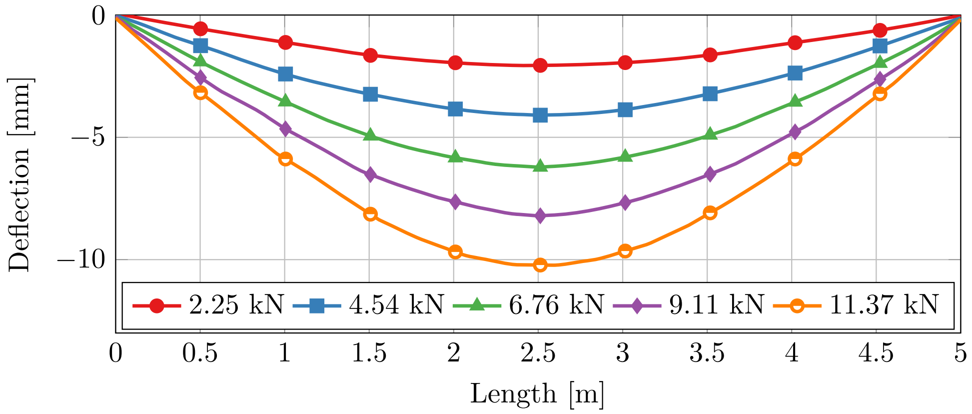

Fig. 14 Deflection profiles at different load levels in the three-point bending test. Data extracted from [39]

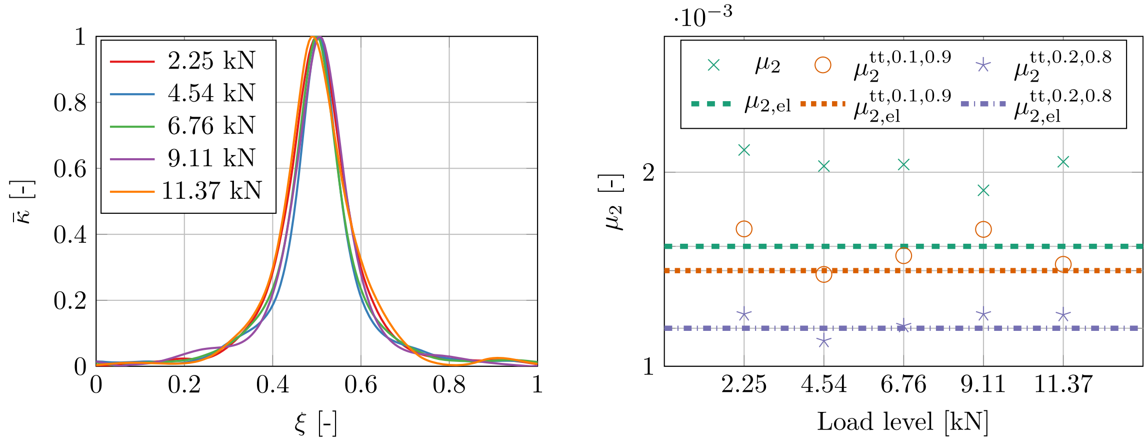

Fig. 15 Normalised curvature, $\bar{\kappa}$ (left), and the computed values of diagnostic indicator, μ_2. Three-point bending test carried out by Yoneyama et al. [39]

3.4 Summary and Discussion

The behaviour of the diagnostic indicator in the elastoplastic range follows similar steps for all studied load cases and different cross-section shapes. In all cases, the constant elastic reference value is observed until the elastic limit load was reached. Then, the indicator rapidly decreases as soon as the plastic limit load is reached. The exact shape of the interim region between the limit loads depends on the relative location of the maximum bending moment with respect to the maximum elastic deflection.

In the general three- and four-point bending cases, the diagnostic indicator does not monotonically decrease with growing load, as observed for uniformly distributed load. Thus, μ_2 can be larger than its elastic reference value. However, even in three- and four-point bending, a monotonic decrease in the μ_2 value can be observed provided that the maximum bending moment is located close enough to the mid-span. From numerical simulations, this was the case when the maximum bending moment was located at $\xi \in (0.41, 0.59)$, which is consistent with the range of the curvature peak locations. In these cases, the diagnostic indicator monotonically decreases with the load and $\mu_{2,el}$ cannot be higher than the elastic reference value. A value lower than the reference indicates that the beam is not in the elastic range.

When μ_2 is monotonically decreasing, it is possible to uniquely identify a plastic reference value, $\mu_{2,pl} < \mu_{2,el}$, which signifies a fully developed plastic hinge and an impending mechanism action upon further increase of the load. As presented in Fig. 7, a different $\mu_{2,pl}$ can be found for different cross-sections.

A value $\mu_2 \in (\mu_{2,el}, \mu_{2,pl})$ indicates that the plastic hinge has not yet fully formed. In this range, the load or stress level can be determined on the basis of the specific value of the diagnostic indicator (upon proper calibration against different cross-section shapes). For the estimation of stress levels below the elastic limit load, other methods have been developed, e.g., Park et al. [33] use a similar deflection analysis to estimate stress levels in the elastic range.

The diagnostic indicator provides a unique description of elastoplastic behaviour of beams as long as the largest bending moment is close enough to the mid-span (or as long as the plastic hinge forms close to the maximum elastic curvature). If that is not the case, the value of diagnostic indicator function is not unique, but it is always possible to monitor whether the beam is working in a post-elastic range.

4 Experimental Validation for Elastic and Post-elastic Range

In this section, the proposed diagnostic framework was implemented and employed in the analysis of a few experiments. All the experiments treated here were found in the existing literature, and involved the monitoring of beam deflection using a digital image correlation (DIC) system. Digital image correlation is a non-contact optical measurement technique that accurately tracks changes in 2D and 3D images. A DIC system uses cross-correlation to measure the similarity between pixel intensity in two or more images captured using digital cameras, enabling the measurement of displacement and strain fields.

Various applications are covered because the studied tests involved three-point bending of short and large steel beams working in the elastic range, as well as the identification of post-elastic damage in a three-point bending test of a gypsum board. First, some implementation guidelines and some details regarding the treatment of noisy experimental data are provided.

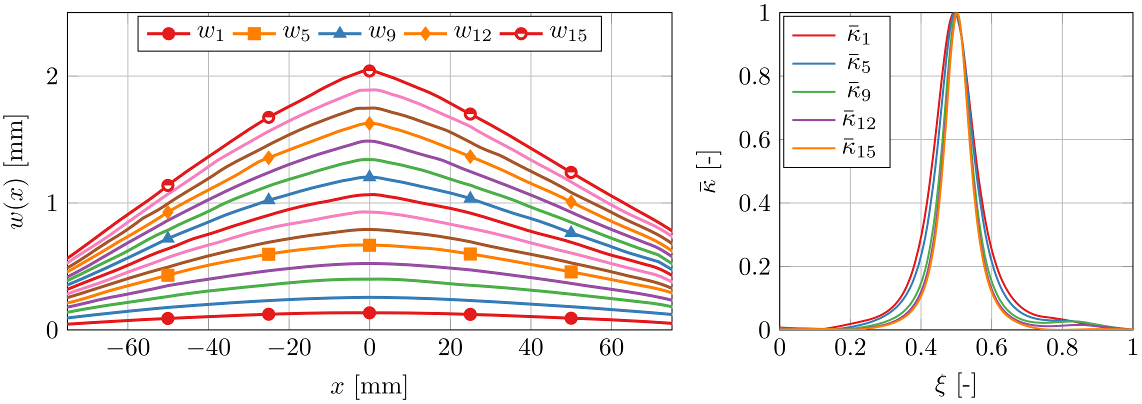

Fig. 16 Deflection profiles for different image frames (left). Data extracted from [40]. Normalised curvature for selected deflection profiles, $\bar{\kappa}$ (right)

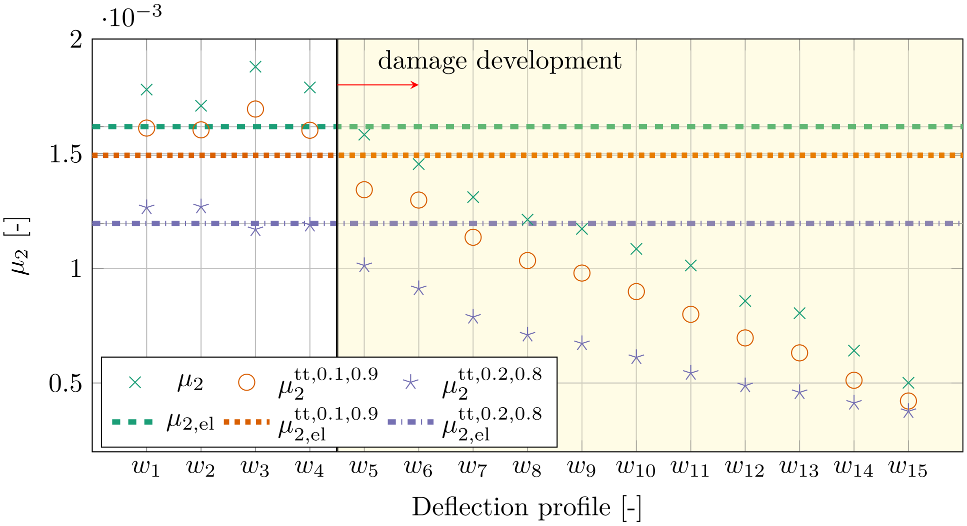

Fig. 17 Diagnostic indicator values, μ_2 for the deflection profiles w_1–w_{15}

4.1 Implementation Guidelines

Although computed numerically, the elastic reference values, $\mu_{2,el}$, were derived from analytical expressions readily available for beams modelled using Euler–Bernoulli assumptions. To calculate the diagnostic indicator, μ_2, it is necessary to compute the second derivative of the deflection function. In practice, analytical expressions are not readily available from measurements. Moreover, once a plastic hinge is formed or a significant amount of damage has occurred, the deflection function cannot be well described with a single polynomial function, as was the case in the elastic range.

From DIC measurements, a set of data points defining the deflection line can be easily extracted. It is then possible to fit a curve describing the observed deflection function. For the best performance, an approach based on spline fitting is suitable. First, by treating the data points as knots, we fit an interpolating basis spline function. As spline interpolation is readily available in most computational packages, it is straightforward to compute derivatives at selected points. Before computation of the curvature function (Eq. 2), a cubic smoothing spline [36, 37] is used to regularise the computed first and second derivatives. For a given data set (x_j, y_j), such smoothing spline f minimises

$$p\sum_{j=1}^{n} w_j\left|y_j - f(x_j)\right|^2 + (1-p)\int \lambda(t)\left|\frac{\mathrm{d}^2 f(t)}{\mathrm{d}t^2}\right|^2 \mathrm{d}t, \qquad (14)$$

where w_j denote the error weights, and $\lambda(t)$ is a weight function for the roughness measure. The first term in Equation 14 measures the error and the second term measures the roughness of the spline. The smoothing parameter, p, can be fine-tuned, so that the risk of overfitting to the data set is mitigated. Setting $p = 0$ results in a least-squares fit to the data. Similarly, setting $p = 1$ results in the natural cubic spline interpolant. This reduces the noise and ensures that the resulting curvature functions are smooth.

4.2 Treatment of Experimental Data

Regions close to supports are particularly sensitive because deformation in these regions is much smaller than in the mid-span. Thus, the data from regions closest to the supports, especially at the initial loading stages, can be noisy. Computing the normalised curvature, $\bar{\kappa}(\xi)$, can result in functions, which tails exhibit a considerable amount of noise. However, as the values of the $\mu_{2,el}$ in Section 2 were integrated from $\xi = 0$ to $\xi = 1$, the comparison with the computed values might not prove meaningful. Thus, it omitting the tails of $\bar{\kappa}(\xi)$ when integrating μ_2 can be practical. These tail-truncated values of the diagnostic indicator, integrated between ξ_1 and ξ_2 are denoted $\mu_2^{\mathrm{tt},\xi_1,\xi_2}$. For a convenient reference, the elastic reference tail-truncated values $\mu_{2,el}^{\mathrm{tt},0.1,0.9}$ and $\mu_{2,el}^{\mathrm{tt},0.2,0.8}$ are reported in Tables 4 and 5, respectively.

4.3 Three-Point Bending of Short Aluminium Rods—Elastic Range

For validation, the test performed in [38] by Farsi et al. was used. In the research presented, a number of three-point bending tests were carried out on short aluminium rods with different porosities. These tests were conducted to accurately determine the mechanical properties of the material (Young's modulus) with the use of DIC analysis.

The three-point bending tests were performed on 20 mm long aluminium bars with a square cross-section (mean side length of 4.63 mm). Given that the span-to-depth ratio of the beam was approximately 4.32, the Euler–Bernoulli beam model should yield reasonable results, However, a framework based on the Timoshenko beam model could possibly provide better results. The force was applied in the middle of the span, and DIC was used to reconstruct deflection profiles for the bars at different load levels. For this study, data points were extracted from available graphs at different load levels (Fig. 12). After obtaining the deflection functions in the form of data points, the described framework was used to compute the pertinent normalised curvatures (Fig. 13 on the left) and diagnostic indicators (Fig. 13 on the right)

It is noteworthy that the material in the test was reported to behave almost as a perfectly elastic material and exhibited brittle failure—no plastic response was recorded. This indicates that the values of the computed diagnostic indicators, μ_2 should be close to the elastic reference values $\mu_{2,el}$ (Fig. 13). Moreover, the tail-truncated values of the diagnostic indicator matched the elastic reference values better due to less tail noise. The computed values were close to theoretical reference values, with a mean error of approximately 1.3% in the case of the tail-truncated indicator $\mu_2^{\mathrm{tt},0.2,0.8}$. This confirms that the behaviour of the beam was elastic.

4.4 Three-Point Bending of Long Steel Beams—Elastic Range

To illustrate the feasibility of using the proposed framework for longer structural elements, three-point bending tests performed by Yoneyama et al. [39] were used. The tests were performed on a 5 m long steel beam with an H-shaped cross-section, loaded in the middle of the span. The height of the cross-section was 200 mm, which resulted in a span-to-depth ratio of 25, justifying the use of the Euler–Bernoulli beam model. In the tests, DIC was used to reconstruct deflection profiles at five different load levels. Although the SS4000 steel used in the test exhibited elastoplastic behaviour, all the tests were conducted only in the elastic regime. The registered deflection profiles reported in the work and used for data point extraction are presented in Fig. 14. The data points were used in the proposed framework to compute normalised curvatures and the values of the diagnostic indicator, μ_2, presented in Fig. 15.

The curvature profiles mostly coincided, especially in the interior of the graph. Noticeable discrepancies were observed between curvature profiles in the exterior regions (close to tails), which are caused by the accuracy of data extraction. The computed values of the indicator, μ_2, followed the same trend, with all values being close to the theoretical reference elastic value, $\mu_{2,el}$. Due to imperfect tails of the curvature profiles, full values of the indicator show some bias, but the tail-truncated values provide a much better match, with a mean error of 2.8% for the tail-truncated reference value $\mu_2^{\mathrm{tt},0.2,0.8}$. The analysis indicated that the beam was working in the elastic range at all load levels.

4.5 Three-Point Bending of Gypsum Boards—Elastic and Post-elastic Range

For the last case, three-point flexure tests performed by Hild et al. [40] on gypsum boards were considered. Although the material does not exhibit elastoplastic properties, the proposed diagnostic method can easily detect the onset of damage. Because the studied material was quasi-brittle, any deviation from the elastic state can be considered as damage. In the mentioned work, the authors utilised DIC techniques to detect defects and quantify damage directly in the volume of the material. However, a separate DIC analysis is also applied to a one-dimensional medium described by the Euler–Bernoulli model, and rich experimental data in terms of deflection profiles both before and after the onset of damage was provided by the authors. Deflection profiles, reconstructed from the extracted data are presented in Figure 16 together with computed normalised curvatures. In total, 15 deflection curves were provided for the sample. For clarity and to illustrate the significance of damage, the normalised curvature, $\bar{\kappa}$, is plotted only for five specific cases, schematically marked in the figure.

The values of the full and tail-truncated diagnostic indicators, μ_2, were computed for all deflection curves, w_1 through w_{15}, and are presented in Fig. 17. Starting from the left, for the first four deflection curves, the indicators were close to the elastic reference values. The tail-truncated values tended to be closer to the reference elastic value, with a mean error of 2.3% for the tail-truncated reference value $\mu_2^{\mathrm{tt},0.2,0.8}$.

Starting from w_5 and beyond, the values of the full and tail-truncated indicators began to monotonically decrease, indicating the onset and development of damage in the beam. This finding agrees with the results in [40], where the authors report a damage parameter equal to 0 for the first four deflection profiles, which then progressively grew for the rest. The decrease in the indicator value can also be concluded from the curvature profiles in Fig. 16, where the curves become thinner as the damage develops, thus reducing the value of μ_2. Moreover, as the damage develops, the variance between the full and tail-truncated indicator values becomes smaller. Thus, all three values are much closer to each other for w_{15}, than they are for w_5. For this experimental case, the performance of the diagnostic framework was illustrated both in the elastic and post-elastic range, where the post-elastic range for this specific quasi-brittle material indicated the onset and development of the damage.

5 Conclusions

In this study, a simple diagnostic method based on deflection analysis for monitoring the post-elastic response of beams was developed. The proposed indicator was defined as the second moment of the normalised curvature function about the mid-span, with the curvature computed from a normalised deflection profile. The application of the method was illustrated by means of finite element simulations and suitable experiments on simply supported beams. In experimental tests, a mean error of 2.1% was obtained between the measured and theoretical values of the diagnostic indicator.

Obtaining indicator values smaller than the reference value indicates that the beam is not working in the elastic range. For quasi-brittle materials, the deviation from the elastic range can usually signify the onset of damage. For elastoplastic materials, the proposed framework allows for the direct monitoring of the post-elastic stress level in the cross-section as long as the value of the indicator is monotonically decreasing with progressive loading. This occurs when the maximum bending moment is located close to the mid-span, i.e., at $\xi \in (0.41, 0.59)$ for the studied load cases.

The main benefit of the proposed diagnostic method is its simplicity because only the shape of the deflection curve is needed. No additional information on the cross-section and material is necessary to compute the indicator. Upon further assumptions, information on the bending stiffness of the cross-section or the load case can be obtained. Furthermore, because the indicator often provides a unique one-number representation of the elastoplastic response, this value can be used as a post-elastic 'state identifier' in experimental investigations.

Appendix A: Elastic Reference Values of the Diagnostic Indicator

The elastic reference values of the full (integrated between $\xi_1 = 0$ and $\xi_2 = 1$, denoted $\mu_{2,el}$) and tail-truncated (integrated between $\xi_1 = 0.1$ and $\xi_2 = 0.9$, as well as between $\xi_1 = 0.2$ and $\xi_2 = 0.8$, denoted $\mu_{2,el}^{tt,0.1,0.9}$ and $\mu_{2,el}^{tt,0.2,0.8}$, respectively) diagnostic indicator are reported in Table 1 for uniformly distributed load, in Table 2 for three-point bending, and in Tables 3, 4 and 5 for four-point bending.

Table 1 The elastic reference values of the full ($\mu_{2,el}$) and tail-truncated ($\mu_{2,el}^{tt,0.1,0.9}$, $\mu_{2,el}^{tt,0.2,0.8}$) diagnostic indicator, uniformly distributed load

$\mu_{2,el}$	2.477×10^{-3}
$\mu_{2,el}^{tt,0.1,0.9}$	2.276×10^{-3}
$\mu_{2,el}^{tt,0.2,0.8}$	1.808×10^{-3}

Table 2 The elastic reference values of the full ($\mu_{2,el}$) and tail-truncated ($\mu_{2,el}^{tt,0.1,0.9}$, $\mu_{2,el}^{tt,0.2,0.8}$) diagnostic indicator, three-point bending

α_1	0.05	0.10	0.15	0.20	0.25	0.30	0.35	0.40	0.45	0.50
$\mu_{2,el}$ ($\times 10^{-3}$)	4.072	3.875	3.612	3.297	2.953	2.602	2.269	1.980	1.757	1.618
$\mu_{2,el}^{tt,0.1,0.9}$ ($\times 10^{-3}$)	3.718	3.610	3.403	3.114	2.785	2.444	2.121	1.839	1.624	1.493
$\mu_{2,el}^{tt,0.2,0.8}$ ($\times 10^{-3}$)	2.994	2.912	2.777	2.595	2.346	2.051	1.759	1.502	1.308	1.196

Table 3 The elastic reference values of the full diagnostic indicator, $\mu_{2,el}$ ($\times 10^{-3}$), four-point bending

	α_1										
α_2	0.00	0.05	0.10	0.15	0.20	0.25	0.30	0.35	0.40	0.45	0.50
0.00	n.a.	4.072	3.875	3.612	3.297	2.953	2.602	2.269	1.980	1.757	1.618
0.05	4.072	4.072	3.942	3.730	3.457	3.145	2.815	2.495	2.210	1.982	1.879
0.10	3.875	3.942	3.875	3.718	3.491	3.216	2.915	2.614	2.338	2.114	2.046
0.15	3.612	3.730	3.718	3.612	3.432	3.197	2.930	2.653	2.394	2.178	2.136
0.20	3.297	3.457	3.491	3.432	3.297	3.105	2.873	2.626	2.389	2.186	2.160
0.25	2.953	3.145	3.216	3.197	3.105	2.953	2.759	2.544	2.332	2.147	2.127
0.30	2.602	2.815	2.915	2.930	2.873	2.759	2.602	2.420	2.235	2.070	2.050
0.35	2.269	2.495	2.614	2.653	2.626	2.544	2.420	2.269	2.112	1.969	1.943
0.40	1.980	2.210	2.338	2.394	2.389	2.332	2.235	2.112	1.980	1.859	1.824
0.45	1.757	1.982	2.114	2.178	2.186	2.147	2.070	1.969	1.859	1.757	1.711
0.50	1.618	1.879	2.046	2.136	2.160	2.127	2.050	1.943	1.824	1.711	1.618
0.55	1.757	2.028	2.190	2.271	2.286	2.243	2.157	2.043	1.920	1.805	1.711
0.60	1.980	2.249	2.397	2.463	2.460	2.401	2.300	2.174	2.041	1.920	1.824
0.65	2.269	2.528	2.655	2.696	2.669	2.587	2.465	2.321	2.174	2.043	1.943
0.70	2.602	2.845	2.942	2.951	2.893	2.781	2.632	2.465	2.300	2.157	2.050
0.75	2.953	3.175	3.234	3.205	3.109	2.961	2.781	2.587	2.401	2.243	2.127
0.80	3.297	3.495	3.509	3.435	3.296	3.109	2.893	2.669	2.460	2.286	2.160
0.85	3.612	3.783	3.745	3.621	3.435	3.205	2.951	2.696	2.463	2.271	2.136
0.90	3.875	4.019	3.922	3.745	3.509	3.234	2.942	2.655	2.397	2.190	2.046
0.95	4.072	4.184	4.019	3.783	3.495	3.175	2.845	2.528	2.249	2.028	1.879
1.00	n.a.	4.072	3.875	3.612	3.297	2.953	2.602	2.269	1.980	1.757	1.618

Table 4 The elastic reference values of the tail-truncated diagnostic indicator, $\mu_{2,el}^{\mathrm{tt},0.1,0.9}$ ($\times 10^{-3}$), four-point bending

	α_1										
α_2	0.00	0.05	0.10	0.15	0.20	0.25	0.30	0.35	0.40	0.45	0.50
0.00	n.a.	3.718	3.610	3.403	3.114	2.785	2.444	2.121	1.839	1.624	1.493
0.05	3.718	3.718	3.646	3.480	3.230	2.931	2.611	2.297	2.018	1.797	1.695
0.10	3.610	3.646	3.610	3.485	3.276	3.011	2.718	2.423	2.153	1.933	1.864
0.15	3.403	3.480	3.485	3.403	3.237	3.011	2.750	2.478	2.225	2.014	1.969
0.20	3.114	3.230	3.276	3.237	3.114	2.929	2.704	2.461	2.229	2.031	2.001
0.25	2.785	2.931	3.011	3.011	2.929	2.785	2.596	2.386	2.178	1.998	1.975
0.30	2.444	2.611	2.718	2.750	2.704	2.596	2.444	2.267	2.086	1.926	1.903
0.35	2.121	2.297	2.423	2.478	2.461	2.386	2.267	2.121	1.967	1.829	1.801
0.40	1.839	2.018	2.153	2.225	2.229	2.178	2.086	1.967	1.839	1.722	1.688
0.45	1.624	1.797	1.933	2.014	2.031	1.998	1.926	1.829	1.722	1.624	1.580
0.50	1.493	1.695	1.864	1.969	2.001	1.975	1.903	1.801	1.688	1.580	1.493
0.55	1.624	1.827	1.992	2.091	2.116	2.082	2.002	1.894	1.776	1.667	1.580
0.60	1.839	2.031	2.184	2.270	2.280	2.230	2.137	2.017	1.891	1.776	1.688
0.65	2.121	2.291	2.425	2.491	2.479	2.407	2.293	2.157	2.017	1.894	1.801
0.70	2.444	2.585	2.693	2.731	2.690	2.591	2.451	2.293	2.137	2.002	1.903
0.75	2.785	2.888	2.964	2.968	2.892	2.760	2.591	2.407	2.230	2.082	1.975
0.80	3.114	3.172	3.210	3.177	3.062	2.892	2.690	2.479	2.280	2.116	2.001
0.85	3.403	3.406	3.406	3.333	3.177	2.968	2.731	2.491	2.270	2.091	1.969
0.90	3.610	3.549	3.516	3.406	3.210	2.964	2.693	2.425	2.184	1.992	1.864
0.95	3.718	3.590	3.549	3.406	3.172	2.888	2.585	2.291	2.031	1.827	1.695
1.00	n.a.	3.718	3.610	3.403	3.114	2.785	2.444	2.121	1.839	1.624	1.493

Table 5 The elastic reference values of the tail-truncated diagnostic indicator, $\mu_{2,el}^{\mathrm{tt},0.2,0.8}$ ($\times 10^{-3}$), four-point bending

	α_1										
α_2	0.00	0.05	0.10	0.15	0.20	0.25	0.30	0.35	0.40	0.45	0.50
0.00	n.a.	2.994	2.912	2.777	2.595	2.346	2.051	1.759	1.502	1.308	1.196
0.05	2.994	2.994	2.939	2.831	2.672	2.446	2.170	1.886	1.630	1.429	1.335
0.10	2.912	2.939	2.912	2.831	2.698	2.499	2.245	1.978	1.729	1.529	1.458
0.15	2.777	2.831	2.831	2.777	2.672	2.501	2.275	2.029	1.794	1.600	1.549
0.20	2.595	2.672	2.698	2.672	2.595	2.454	2.258	2.037	1.821	1.639	1.601
0.25	2.346	2.446	2.499	2.501	2.454	2.346	2.182	1.990	1.797	1.631	1.600
0.30	2.051	2.170	2.245	2.275	2.258	2.182	2.051	1.890	1.723	1.576	1.547
0.35	1.759	1.886	1.978	2.029	2.037	1.990	1.890	1.759	1.618	1.492	1.461
0.40	1.502	1.630	1.729	1.794	1.821	1.797	1.723	1.618	1.502	1.396	1.362
0.45	1.308	1.429	1.529	1.600	1.639	1.631	1.576	1.492	1.396	1.308	1.268
0.50	1.196	1.335	1.458	1.549	1.601	1.600	1.547	1.461	1.362	1.268	1.196
0.55	1.308	1.441	1.556	1.641	1.689	1.683	1.625	1.535	1.434	1.340	1.268
0.60	1.502	1.614	1.714	1.786	1.824	1.807	1.739	1.640	1.531	1.434	1.362
0.65	1.759	1.839	1.915	1.969	1.989	1.957	1.872	1.759	1.640	1.535	1.461
0.70	2.051	2.088	2.134	2.163	2.163	2.109	2.003	1.872	1.739	1.625	1.547
0.75	2.346	2.329	2.339	2.341	2.316	2.238	2.109	1.957	1.807	1.683	1.600
0.80	2.595	2.513	2.489	2.467	2.419	2.316	2.163	1.989	1.824	1.689	1.601
0.85	2.777	2.620	2.571	2.533	2.467	2.341	2.163	1.969	1.786	1.641	1.549
0.90	2.912	2.665	2.615	2.571	2.489	2.339	2.134	1.915	1.714	1.556	1.458
0.95	2.994	2.665	2.665	2.620	2.513	2.329	2.088	1.839	1.614	1.441	1.335
1.00	n.a.	2.994	2.912	2.777	2.595	2.346	2.051	1.759	1.502	1.308	1.196

Acknowledgements Financial support of this study from Gdańsk University of Technology by the DEC-2/2020/IDUB/I.1 grant under the Nobelium Joining GUT Research Community programme is gratefully acknowledged.

Data availability Raw data that support the findings of this study are available on request from the corresponding author.

Declarations

Conflict of interest The author declares that they have no known competing financial interests or personal relationships that could have appeared to influence the work reported in this paper.

References

1. Štok B, Halilovič M (2009) Analytical solutions in elasto-plastic bending of beams with rectangular cross section. Appl Math Model 33(3):1749–1760. https://doi.org/10.1016/j.apm.2008.03.011
2. Xi F, Liu F, Li QM (2012) Large deflection response of an elastic, perfectly plastic cantilever beam subjected to a step loading. Int J Impact Eng 48:33–45. https://doi.org/10.1016/j.ijimpeng.2011.05.006
3. Solyaev Y, Lurie S, Prokudin O et al (2020) Elasto-plastic behavior and failure of thick GLARE laminates under bending loading. Compos Part B Eng 200(108):302. https://doi.org/10.1016/j.compositesb.2020.108302
4. Ono R, Ha TM, Fukada S (2019) Analytical study on damage detection method using displacement influence lines of road bridge slab. J Civ Struct Health Monit 9(4):565–577. https://doi.org/10.1007/s13349-019-00352-9
5. Park KT, Kim SH, Park HS et al (2005) The determination of bridge displacement using measured acceleration. Eng Struct 27(3):371–378. https://doi.org/10.1016/j.engstruct.2004.10.013
6. Nassif HH, Gindy M, Davis J (2005) Comparison of laser Doppler vibrometer with contact sensors for monitoring bridge deflection and vibration. NDT & E Int 38(3):213–218. https://doi.org/10.1016/j.ndteint.2004.06.012
7. Lee BH, Kim YH, Park KS et al (2012) Interferometric fiber optic sensors. Sensors. https://doi.org/10.3390/s120302467
8. Inaudi D, Vurpillot S, Casanova N et al (1998) Structural monitoring by curvature analysis using interferometric fiber optic sensors. Smart Mater Struct 7(2):199–208. https://doi.org/10.1088/0964-1726/7/2/007
9. Marković MZ, Bajić JS, Batilović M et al (2019) Comparative analysis of deformation determination by applying fiber-optic 2D deflection sensors and geodetic measurements. Sensors. https://doi.org/10.3390/s19040844
10. Hong W, Lv Z, Zhang X et al (2020) Displacement shape measurement of continuous beam bridges based on long-gauge fiber optic sensing. Opt Fiber Technol 56(102):178. https://doi.org/10.1016/j.yofte.2020.102178
11. Bajić JS, Marković MZ, Joža A et al (2017) Design calibration and characterization of a robust low-cost fiber-optic 2D deflection sensor. Sens Actuators A Phys 267:278–286. https://doi.org/10.1016/j.sna.2017.10.014
12. Abbiati P, Casciati F, Merlo S (2000) An optical fibre sensor for dynamic structural response monitoring. J Struct Control 7(1):35–49. https://doi.org/10.1002/stc.4300070104
13. Zhang Q, Zhang J, Duan W et al (2018) Deflection distribution estimation of tied-arch bridges using long-gauge strain measurements. Struct Control Health Monit 25(3):e2119. https://doi.org/10.1002/stc.2119
14. Pan B, Qian K, Xie H et al (2009) Two-dimensional digital image correlation for in-plane displacement and strain measurement: a review. Meas Sci Technol 20(6):62001. https://doi.org/10.1088/0957-0233/20/6/062001
15. Chiorean R, Dudescu C, Pustan M et al (2014) Deflection determination of V-beam thermal sensors using digital image correlation. Key Eng Mater 601:41–44. https://doi.org/10.4028/www.scientific.net/KEM.601.41
16. Xie X, Grace N, Kasabasic M et al (2018) An application of digital image correlation (DIC) method in large-scale I-beams bending test. https://doi.org/10.4271/2018-01-1218
17. Nunes LCS (2015) Simple approach for 2D-DIC with dual field of view. Meas Sci Technol 26(9):95–205. https://doi.org/10.1088/0957-0233/26/9/095205
18. Lee JJ, Shinozuka M (2006) A vision-based system for remote sensing of bridge displacement. NDT & E Int 39(5):425–431. https://doi.org/10.1016/j.ndteint.2005.12.003
19. Obiechefu CB, Kromanis R (2021) Damage detection techniques for structural health monitoring of bridges from computer vision derived parameters. Struct Monit Maint 8(1):91–110. https://doi.org/10.12989/smm.2021.8.1.091
20. Xu Y, Brownjohn J, Kong D (2018) A non-contact vision-based system for multipoint displacement monitoring in a cable-stayed footbridge. Struct Control Health Monit 25(5):e2115. https://doi.org/10.1002/stc.2155
21. Dworakowski Z, Kohut P, Gallina A et al (2016) Vision-based algorithms for damage detection and localization in structural health monitoring. Struct Control Health Monit 23(1):35–50. https://doi.org/10.1002/stc.1755
22. Khuc T, Catbas FN (2017) Completely contactless structural health monitoring of real-life structures using cameras and computer vision. Struct Control Health Monit 24(1):18–52. https://doi.org/10.1002/stc.1852
23. Lee HM, Park HS (2011) Gage-free stress estimation of a beam-like structure based on terrestrial laser scanning. Comput Aided Civ Infrastruct Eng 26(8):647–658. https://doi.org/10.1111/j.1467-8667.2011.00723.x
24. Park SW, Park HS, Kim JH et al (2015) 3D displacement measurement model for health monitoring of structures using a motion capture system. Measurement 59:352–362. https://doi.org/10.1016/j.measurement.2014.09.063
25. Park J, Sim S, Jung H (2013) Displacement estimation using multimetric data fusion. IEEE/ASME Trans Mechatron 18(6):1675–1682. https://doi.org/10.1109/TMECH.2013.2275187
26. Elhattab A, Uddin N, OBrien E (2016) Drive-by bridge damage monitoring using bridge displacement profile difference. J Civ Struct Health Monit 6(5):839–850. https://doi.org/10.1007/s13349-016-0203-6

27. Chen ZW, Cai QL, Zhu S (2018) Damage quantification of beam structures using deflection influence lines. Struct Control Health Monit 25(11):e2242. https://doi.org/10.1002/stc.2242
28. RaghuPrasad BK, Lakshmanan N, Gopalakrishnan N et al (2013) Damage identification of beam-like structures with contiguous and distributed damage. Struct Control Health Monit 20(4):496–519. https://doi.org/10.1002/stc.511
29. Dincal S, Stubbs N (2014) Nondestructive damage detection in Euler–Bernoulli beams using nodal curvatures—part I: theory and numerical verification. Struct Control Health Monit 21(3):303–316. https://doi.org/10.1002/stc.1562
30. Martinez D, Malekjafarian A, OBrien E (2020) Bridge health monitoring using deflection measurements under random traffic. Struct Control Health Monit 27(9):25–93. https://doi.org/10.1002/stc.2593
31. Sun Z, Nagayama T, Fujino Y (2016) Minimizing noise effect in curvature-based damage detection. J Civ Struct Health Monit 6(2):255–264. https://doi.org/10.1007/s13349-016-0163-x
32. Yang M, Zhong H, Telste M et al (2016) Bridge damage localization through modified curvature method. J Civ Struct Health Monit 6(1):175–188. https://doi.org/10.1007/s13349-015-0150-7
33. Park JS, Oh BK, Choi SW et al (2016) Sensor-free stress estimation model for steel beam structures using a motion capture system. IEEE Sens J 16(8):2701–2713. https://doi.org/10.1109/JSEN.2016.2519033
34. Deng Y, Li A, Chen S et al (2018) Serviceability assessment for long-span suspension bridge based on deflection measurements. Struct Control Health Monit 25(11):e2254. https://doi.org/10.1002/stc.2254
35. Ha TM, Fukada S (2017) Nondestructive damage detection in deteriorated girders using changes in nodal displacement. J Civ Struct Health Monit 7(3):385–403. https://doi.org/10.1007/s13349-017-0231-x
36. De Boor C (1978) A practical guide to splines, vol 27. Applied mathematical sciences. Springer, New York
37. Craven P, Wahba G (1978) Smoothing noisy data with spline functions. Numerische Mathematik 31(4):377–403. https://doi.org/10.1007/BF01404567
38. Farsi A, Pullen AD, Latham JP et al (2017) Full deflection profile calculation and Young's modulus optimisation for engineered high performance materials. Sci Rep 7(1):46–190. https://doi.org/10.1038/srep46190
39. Yoneyama S, Kitagwa A, Kitamura K, et al (2005) Deflection distribution measurement of steel structure using digital image correlation. In: Hanssen LM, Farrell PV (eds) Optical diagnostics, pp 133–140. https://doi.org/10.1117/12.614364
40. Hild F, Bouterf A, Roux S (2015) Damage measurements via DIC. Int J Fract 191(1):77–105. https://doi.org/10.1007/s10704-015-0004-7